2015

Mechanical properties of self-assembled nanoparticle membranes: stretching and bending

Yifan Wang

Pongsakorn Kanjanaboos

Sean P. McBride
Marshall University, mcbrides@marshall.edu

Edward Barry

Xiao-Min Lin

See next page for additional authors

Authors

Yifan Wang, Pongsakorn Kanjanaboos, Sean P. McBride, Edward Barry, Xiao-Min Lin, and Heinrich M. Jaeger

Mechanical properties of self-assembled nanoparticle membranes: stretching and bending

Yifan Wang[1,2,*], Pongsakorn Kanjanaboos[1,2], Sean P. McBride[2], Edward Barry[3], Xiao-Min Lin[3] and Heinrich M. Jaeger[1,2]

[1] Department of Physics, University of Chicago, 5720 S. Ellis Avenue, Chicago, Illinois 60637, United States

[2] James Franck Institute, University of Chicago, 929 E. 57th Street, Chicago, Illinois 60637, United States

[3] Center for Nanoscale Materials, Argonne National Laboratory, 9700 South Cass Avenue, Argonne, Illinois 60439, United States

Abstract

Monolayers composed of colloidal nanoparticles, with thickness less than ten nanometers, have remarkable mechanical strength and can suspend over micron-sized holes to form free-standing membranes. We discuss experiments probing the tensile strength and bending stiffness of these self-assembled nanoparticle sheets. The fracture behavior of monolayers and multilayers is investigated by attaching them to elastomer substrates which are then stretched. For different applied strain the fracture patterns are imaged down to the scale of single particles. The resulting detailed information about the crack width distribution allows us to relate the measured overall tensile strength to the distribution of local bond strengths within a layer. We then introduce two methods by which freestanding nanoparticle monolayers can be rolled up into hollow, tubular "nano-scrolls", either by electron beam irradiation during imaging with a scanning electron microscope or by spontaneous self-rolling. Indentation measurements on the nano-scrolls yield values for the bending stiffness that are significantly larger than expected from the response to stretching. The ability to stretch, bend, and roll up nanoparticle sheets offers new possibilities for a variety of applications, including sensors and mechanical transducers.

1. Introduction

In recent years, nanoparticle-based solids formed from metallic or semiconducting particle cores capped with short organic ligands have attracted much interest, as they combine the specific optical, electronic or magnetic functionality of nanoparticles with the flexibility of self-assembly[1-13]. In these solids, nanoparticles serve as "artificial atoms" and a particularly interesting limit occurs when they form monolayers, i.e., when the material thickness is reduced to the size of an individual "atom." The mechanical properties of such monolayers have shown a number of remarkable features, including Young's moduli of several GPa and the ability to form freestanding membranes that can stretch across holes or trenches that are hundreds to thousands of particle diameters wide. These are fundamentally new types of two-dimensional (2D) materials in the sense that both the inorganic nanoparticle core and organic capping ligand can be tuned independently with almost unlimited possibilities, a distinct advantage over other 2D systems such as graphene[14]. In contrast to truly atomic 2D systems, in which covalent and ionic bonding provides the mechanical stability, the interactions between nanoparticles can have multiple origins and occur over a much longer length scale[15]. This introduces new possibilities and also a number of interesting questions that still remain to be answered in detail, in particular concerning the ultimate strength of such membranes and the extent to which in-plane stretching and out-of-plane bending can be related. Underlying these questions is a larger issue, namely whether classical elastic membrane theory can properly describe the behavior of nanoparticle-based solids when one or more dimensions approach the size of the discrete building blocks. Here we discuss experiments that address some of these aspects.

As a new functional material which could have potential applications in filtration, mechanical resonators and flexible electronics[16-18], it is important to know its fracture limit under tension[19-24]. More importantly, from knowledge about how the material fails when stretched, we can extract rich information about the interactions between particles, as mediated by the ligands. In our system, the fabrication of nanoparticle monolayers and multilayers is relatively straightforward by self-assembly at a liquid-air interface. For the experiments on tensile strength we fabricate samples via sequential deposition one monolayer at a time onto an elastomer substrate. Controlled amounts of strain are applied to the nanoparticle layer by stretching the substrate. The resulting fracture patterns can be imaged down to the resolution of individual

particles using a scanning electron microscope (SEM) or transmission electron microscope (TEM). Statistical analysis of the fracture patterns then gives us information about the intrinsic mechanical strength set by the ligands between nanoparticles. In comparison, it is a much more challenging task to image failure mechanisms down to the atomic level in ordinary solids[25].

The ability to drape nanoparticle monolayers across holes or trenches so they form freestanding membranes provides unique opportunities for investigating the response to out-of-plane bending. We recently discovered[26] that an asymmetry develops between the two faces of gold-dodecanethiol nanoparticle layers when they are self-assembled at an air-water interface under conditions where the ligand packing density on the particle cores is lower than the maximum. The asymmetry consists of slightly fewer ligands occupying the water-facing side of the monolayer as compared to the air-facing side. In most cases, this asymmetry by itself is not sufficient to drive spontaneous curling up of a membrane toward the side originally facing the water once the stress is relieved that keeps the membrane tautly stretched across a hole or trench. Indeed, when freestanding membranes have ripped we find portions that spontaneously have bent to either side, likely depending on the precise details of the process that caused the ripping. However, when we use the electron beam from an electron microscope to irradiate a freestanding membrane we induce strain that greatly amplifies the asymmetry.

We demonstrate how e-beam irradiation can be used to bend sections of a nanoparticle membrane in a highly controlled manner toward the originally water-facing side, making it possible fold membranes and roll them up into three-dimensional structures: hollow nano-scrolls. While this approach offers control, it uses large exposure doses, which makes it slow and furthermore modifies the ligands through a combination of cutting and cross-linking[27-29]. Alternatively, spontaneous self-rolling can be achieved by carefully adjusting the ligand concentration together with the draping and drying conditions. This produces nano-scrolls whose ligands have not been modified by exposure to an electron beam. Measurements of the indentation response then provide values for the membrane bending stiffness that can be compared directly to measurements of the stretching stiffness from prior work[30,31]. We show that the bending stiffness extracted this way is significantly larger than predicted by macroscopic continuum elastic theory. Such enhanced bending rigidity implies enhanced robustness for nanoparticle-based hollow structures, which is a desirable feature for potential applications.
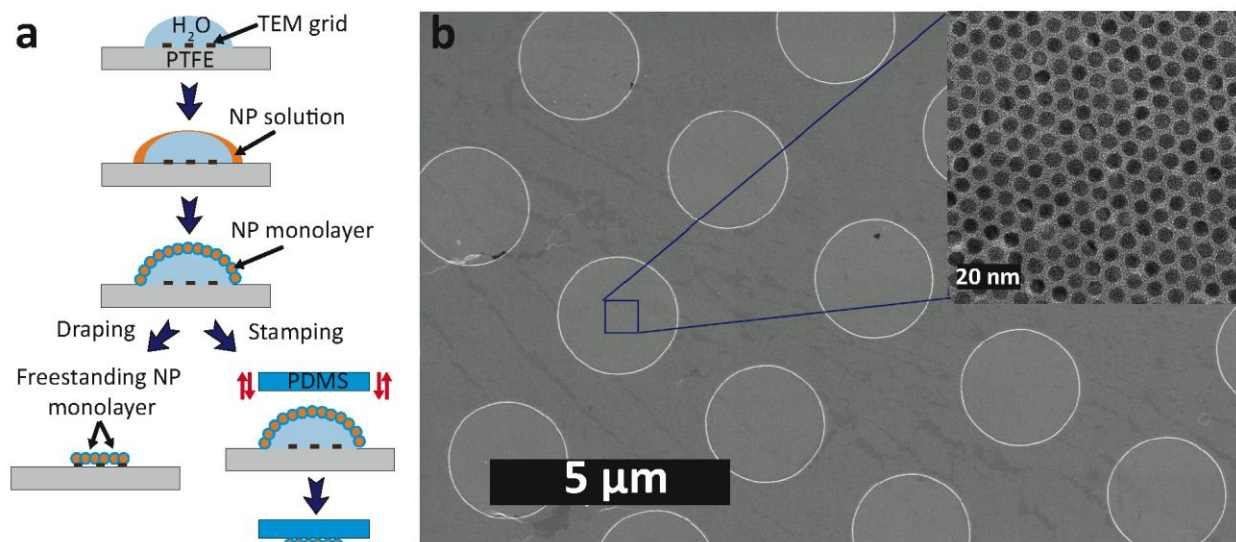
Figure 1. (a) Sketch of nanoparticle monolayer self-assembly on air-water interface and the formation of freestanding monolayer on a TEM grid after water has evaporated. (b) SEM image of freestanding nanoparticle monolayers on carbon-coated TEM grid with array of circular holes. Inset: zoomed in detail of region within freestanding membrane measured by TEM.

2. Nanoparticle synthesis and assembly

In our experiments, Au nanoparticles with ~5.2 nm core diameter were synthesized using a digestive ripening method[16,30-32] , followed by extensive washing with ethanol and finally dissolving in toluene. Au nanoparticles with ~9.1 nm core diameter were synthesized with citrate reduction in water and subsequently transferred into organic solvents[33]. In all cases, the Au nanoparticle cores were stabilized with dodecanethiol ligands. The particles were kept as concentrated solutions, suspended either in toluene or chloroform.

To assemble a nanoparticle monolayer, 30µl of the concentrated nanoparticle solution was deposited around the perimeter of a 300µl distilled water drop (>18 MΩ) on a flat hydrophobic surface, such as polytetrafluoroethylene (PTFE). The nanoparticles climb quickly to the top of the water drop and form a close-packed monolayer at the water-air interface (Fig.1a). The monolayer can then be transferred to different substrates either by letting the water evaporate so the layer drapes itself onto a substrate pre-immersed inside the water drop, or by stamping the particles directly off the water-air interface by touching it with a substrate (Fig. 1a). A variation

of the draping technique situates the water drop not on a flat surface but inside a PTFE cone-shaped support, with the substrate at the bottom (details are discussed in the section on bending).

Remarkably, as shown in Fig. 1b, freestanding monolayers can be fabricated by the draping process. In this specific case, the substrate was a carbon-coated TEM grid with a prefabricated array of 2μm diameter holes. The inset to Fig. 1b shows how freestanding monolayers can maintain good local order.

To assemble nanoparticle multilayers, we used a deposition process in which we applied the stamping technique several times to transfer nanoparticle monolayers from the drop surface to the substrate. The number of layers assembled in this case was simply the number of stamping processes applied.

3. Results and discussion

Stretching and fracture

When slightly indenting a taut freestanding monolayer near its center with an atomic force microscopy (AFM), the response is dominated by tension, similar to what is found when indenting a drumhead. From this response, the Young's modulus can be obtained[30,31]. However, to go far beyond linear response and extract the tensile strength, a setup that can apply strain ε uniformly across a monolayer is more appropriate. To study the fracture behavior more systematically, we therefore moved to experiments as sketched in Fig. 2a.

We used polydimethylsiloxane (PDMS) substrates to stamp monolayers off the air-water interface. These substrates were fabricated by mixing the base and curing agent (SYLGARD 184, Fisher Scientific) with a 7:1 ratio, degassing for 30 minutes, and curing at 70 °C for an hour. The resulting clear elastomer was then cut into 60mm x 15mm x 5mm substrates that were large enough to be mounted in a tensile tester (Instron 5869) for applying controlled amounts of strain after the monolayers had been deposited. While in their final strained state, the monolayers were transferred from the PDMS onto silicon substrates by gently contacting the silicon surface to the PDMS. The hard, slightly conducting silicon surface enabled detailed SEM and AFM imaging of the nanoparticle configurations and crack patterns, without having to worry about

charging effects or substrate compliance. Three different samples at each strain value ε were analyzed and more than 20 SEM images of crack patterns were examined for each sample. In the following discussion, "fracture" refers only to the fracture of the nanoparticle monolayers and multilayers, since the fracture of the PDMS substrates did not occur at the strain values used.
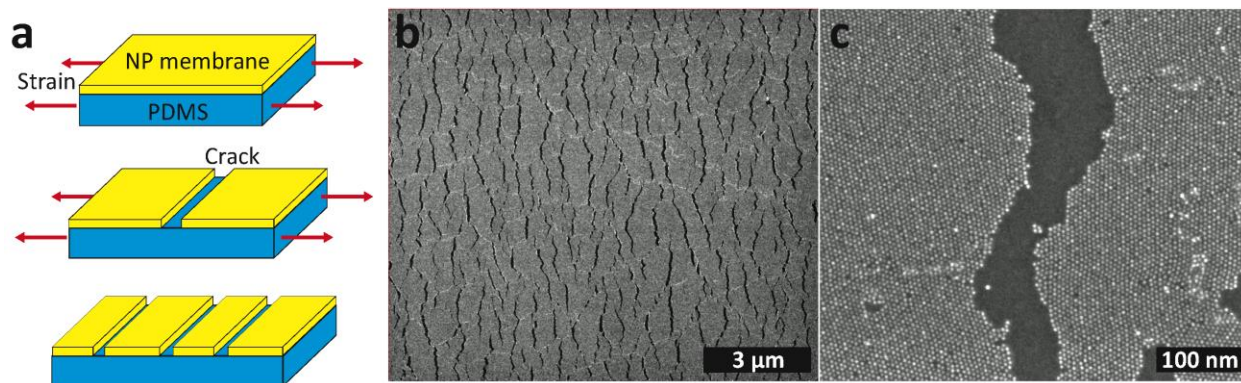

Figure 2. (a) Sketch of nanoparticle membranes deposited onto PDMS substrates, showing crack formation under applied tensile strain. (b) SEM image of crack formation in 5.2 nm Au-dodecenthiol nanoparticle monolayer under the applied strain of 20%. (c) Zoomed in image of a particular crack, making it possible to identify individual nanoparticles. Images (b) and (c) were taken by SEM after the strained monolayer had been transferred from the PDMS to a silicon substrate.

Typical SEM images of fractured monolayers comprised of 5.2nm Au nanoparticles capped with dodecanethiol ligands are shown in Fig. 2 b-c. As we can see in these figures, the as-deposited layers are highly uniform and ordered over distances of ~10 particle lengths, forming local polycrystalline regions separated by grain boundaries. Fig 2b shows that cracks with characteristic spacing appear after stretching. By further zooming in (Fig. 2c), one can see that the crack edges do not necessarily follow the local lattice orientation. Fracture patterns of monolayers stretched to different strains are shown in Fig. 3. At lower strains (<15%), the cracks appear to be long and straight, and run almost perpendicular to the (horizontal) straining direction, while at larger strains (>15%) shorter, zigzag shaped cracks start to appear.

To analyze these fracture patterns quantitatively, the SEM images were scanned line by line to identify the widths, L, of monolayer fragments, and these widths were averaged to obtain the average fragment width $\overline{L}$ for a given strain value. The onset strain for cracking, ε_0, was determined by the intercept in a plot of the inverse average fragment length versus the applied strain ε (Fig. 3, inset c). This onset strain includes two parts: any initial pre-strain within the substrate and the critical strain at which the monolayers show first signs of local fracture[34,35]. The initial pre-strain in the substrate was caused by a slight squeezing of the ends of the PDMS strip when it was mounted in the Instron's test fixture. This pre-strain was about 0.7%, as estimated by measuring the macroscopic curvature of the slightly bent PDMS substrate before a test. This implies a critical strain for fracture onset $\varepsilon_0 \approx 0.9\%$ in our samples. The average fragment width for strains beyond the onset strain ε_0 is plotted in Fig. 3. This width can be fit well by an inversely proportional relationship (red line).
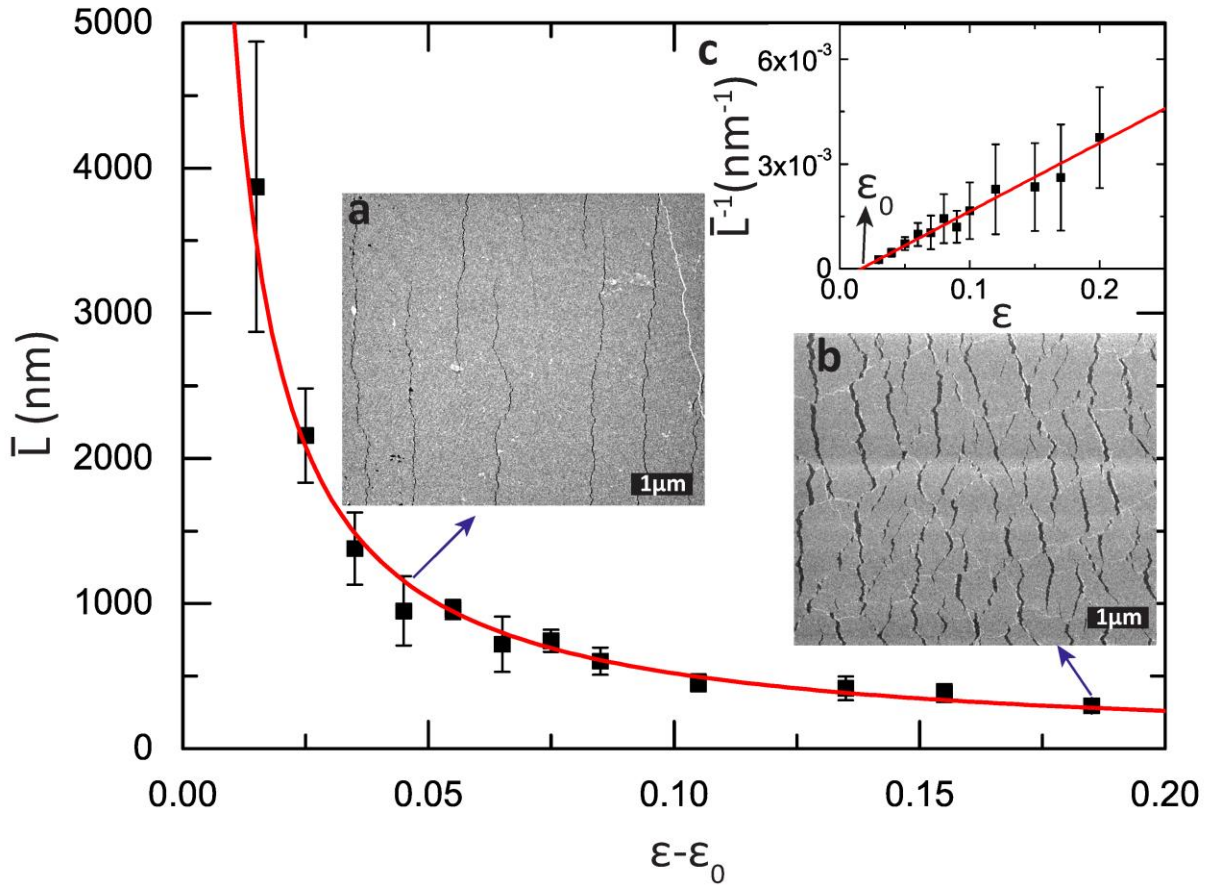
Figure 3. Average fragment width $\bar{L}$ as function of strain $\varepsilon - \varepsilon_0$ for 5.2 nm Au-dodecanethiol nanoparticle monolayers. Here ε_0 is the onset strain (see text). The two SEM images show the crack patterns for 6%(a) and 20%(b) strain. Inset c: Determination of the onset strain ε_0.

To understand this scaling of the fracturing behavior, we use a shear-lag model for the spatial distribution of stress in the monolayer[36-39]. At the very early stages of stretching, initial cracks appear at residual deposition defects or occasional multi-particle voids in the monolayer. This sets the largest possible crack width. Upon further stretching, because of the large mismatch between the elastic modulus of the nanoparticle monolayer and the underlying PDMS substrate, shear zones appear at each end, which transfer tensile stress from the substrate to the monolayer. The length of a shear zone is given by[36,38]

$$L_s \approx 2h_f E_f / E_s \qquad (1)$$

where h_f is the film (here: monolayer) thickness, and E_f and E_s are the Young's moduli of the film and the PDMS substrate, respectively. In our case, this gives $L_s > 10\mu m$, which is larger than the largest fragment width observed in the experiment (~4µm). This means that the tensile stress always reaches its maximum at the fragment center, so that the fragment tends to crack at its midpoint once the tensile stress exceeds σ^*, the fracture stress of the monolayer. Every time the strain doubles, each of the fragments will crack again at its center, resulting in an inversely proportional relationship[29] between the width $\bar{L}$ and the applied strain $\varepsilon - \varepsilon_0$:

$$\bar{L} = \frac{2h_f \sigma^*}{E_s(\varepsilon - \varepsilon_0)} \qquad (2)$$

From a fit to equation 2 we obtain $\sigma^* = 11 \pm 2.6$ MPa for 5.2nm Au nanoparticles. This value represents the average strength towards inducing fracture in a monolayer. Since the nanoparticles are interacting via the interpenetration of shells of short, alkanethiol ligands with no cross-linking at all, the fact that this fracture strength is comparable to cross-linked polymer films is remarkable.

The shear lag model in its simplest form as discussed so far is of course an idealization. Instead of long and straight cracks with equal spacing as predicted by the model, in the actual experiments the cracks are relatively short and exhibit a distribution of width values around the average. The fact that the cracks do not evolve into long, straight channel cracks as in brittle

films[22,23] can be attributed to ductility at the crack tips. This indicates that the monolayer behavior at the local, few-particle length scale can be quite different from that at more macroscopic scales. It also corroborates what we have seen previously when slits were cut with a focused ion beam into freestanding monolayers: the local particle configuration around the tips of the slits can be deformed significantly under stress[35]. Finally, the unequal fragment widths are an indication of variation in the strength with which ligands connect neighboring particles.

To gain a better understanding of how this local bond strength variation generates the distribution of fragment widths, we consider a one-dimensional model. It consists of a chain of particles with the local bond strength between neighbors picked from a Gaussian distribution with mean value σ^* and standard deviation $\Delta\sigma$. From simulation of this model we find that the resulting fragment widths best reproduce the experimental data when a standard deviation $\Delta\sigma \approx$ 3.6MPa is used. This wide distribution in the bond strength between nanoparticles can be understood as arising from a combination of factors, including local lattice defects as well as variation in interparticle spacing and ligand coverage of individual particles[40]. In future work it would be interesting to investigate how better long-range order can decrease the width of this distribution and increase the overall fracture strength of the nanoparticle layer. Since the fracture strength ultimately derives from the degree to which ligand shells belonging to neighboring particles can interpenetrate, one approach to change this interpenetration is to change the nanoparticle size, and thus the curvature of the nanoparticle surface. We anticipate that larger particles will give higher fracture strength, since both the smaller curvature and enhanced van der Waals interaction between the nanoparticle cores could enhance the degree of ligand interpenetration. To prove this hypothesis, monolayers of particles with larger size, 9.1±0.5nm, were fabricated and their fracture strength analyzed using the method just described. The fracture strength $\sigma^* = 15\pm1.7$MPa found in these monolayers is about 40% higher than for monolayers made from the same ligands but using the smaller, 5.2nm diameter Au cores.

The same approach also allows us to analyze the fracture strength of multilayers of nanoparticles, fabricated via sequential deposition one monolayer at a time. Plotting the average fragment widths against strain in Fig. 4a, we find that equation 2 still holds as the number n of layers is increased. In this figure the fragment widths are given in dimensionless form,

normalized by the PDMS substrate modulus E_s and the multilayer film thickness h_f (which is n times the monolayer thickness).
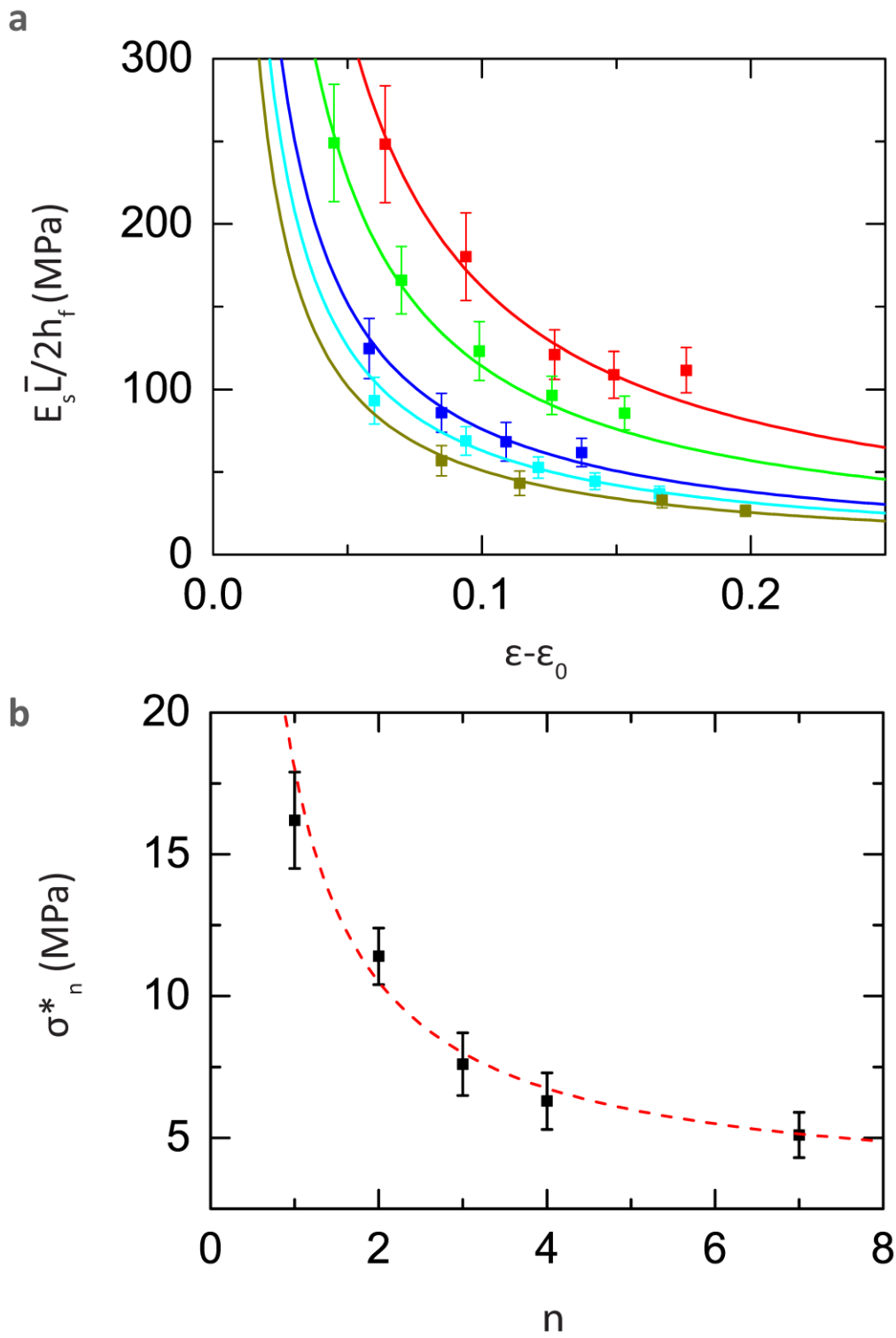
Figure 4. (a) Normalized fragment width as a function of strain beyond onset for multilayers of 9.1 nm Au-dodecanethiol nanoparticles. Solid lines indicating power laws with exponent -1, as in Eq.2. (b) Dependence of the effective fracture strength σ_n^* on film thickness, parameterized by the number n of deposited monolayers.

Immediately apparent is that the fracture strength σ_n^* decreases with increasing number of layers over the range explored from n=1 to n=7 (Fig. 4b). Similar behavior has been observed before in thin metal coatings grown on substrates, where it is usually attributed to larger initial defects in thicker films[41]. Given our multilayer fabrication process, the initial defect sizes are not expected to change with different number of layers. Instead, we believe the behavior seen in Fig. 4 comes from slight differences in residual pre-stress. The first monolayer is deposited directly onto the PDMS substrate, while all subsequent monolayers are deposited onto other monolayers. The fact that the effective, net fracture strength decreases implies that, upon fracture, the $2^{nd} - n^{th}$ layers have taken up proportionally less stress than the first layer. This can happen if the upper layers start out at some residual stress level that is lower than that of the first layer. After the stress in the first monolayer reaches the fracture stress σ^*, the fracture will propagate up across the full film thickness $h_f = nh_0$, where h_0 is the monolayer thickness. If we assume the residual stress in the first layer is larger by an amount $\Delta\sigma_r$, we find that the effective fracture strength for the n layer system follows

$$\sigma_n^* = \frac{\sigma^* h_0 + (n-1)(\sigma^* - \Delta\sigma_r)h_0}{nh_0} = \sigma^* - \Delta\sigma_r + \frac{\Delta\sigma_r}{n} \tag{3}$$

This result matches well with the experimental data when $\Delta\sigma_r = 0.8\ \sigma^* \approx 12$MPa (Fig. 4b red line), implying a residual pre-strain difference $\Delta\varepsilon_r = \Delta\sigma_r / E_f$ of no more than 0.3%.

Bending and folding

One very interesting aspect of freestanding nanoparticle membranes is they can bend, fold or curl easily when they are not stretched flat, simply because they are so very thin. Here we discuss two aspects: How to start with initially flat membranes produced by our draping process and

transform them into simple three-dimensional structures, and how to use nano-scrolls to determine the bending stiffness of nanoparticle monolayers.

Quite generally, for a flat sheet to bend or curl up spontaneously, there has to be a gradient in strain between its top and bottom face. In our monolayers, such strain gradient can arise from an asymmetric ligand distribution that develops while the nanoparticles self-assemble at the water-air interface[18]. As mentioned in the introduction, this gradient often is not significant enough to spontaneously produce large curvature, but it can be amplified very significantly by exposing a freestanding monolayer to an electron beam, for example during SEM or TEM imaging. It is known that electron beams can cause C-H, C-C, and C-S bond cleavage, leading to the formation of C=C bonds and cross-links in the monolayer[28,29]. This in turn pulls particles closer together, effectively introducing internal strain[27]. We note that in all these cases, e-beam exposure will bend the monolayer toward the side that originally faced the water. This is the side of the monolayer that exhibits the slightly lower ligand density and that therefore can contract slightly more under e-beam exposure, as sketched in Fig. 5a1. Since the monolayer is sufficiently thin, the beam will always penetrate fully and it is therefore irrelevant which of the two sides of the layer is facing the e-beam.

13
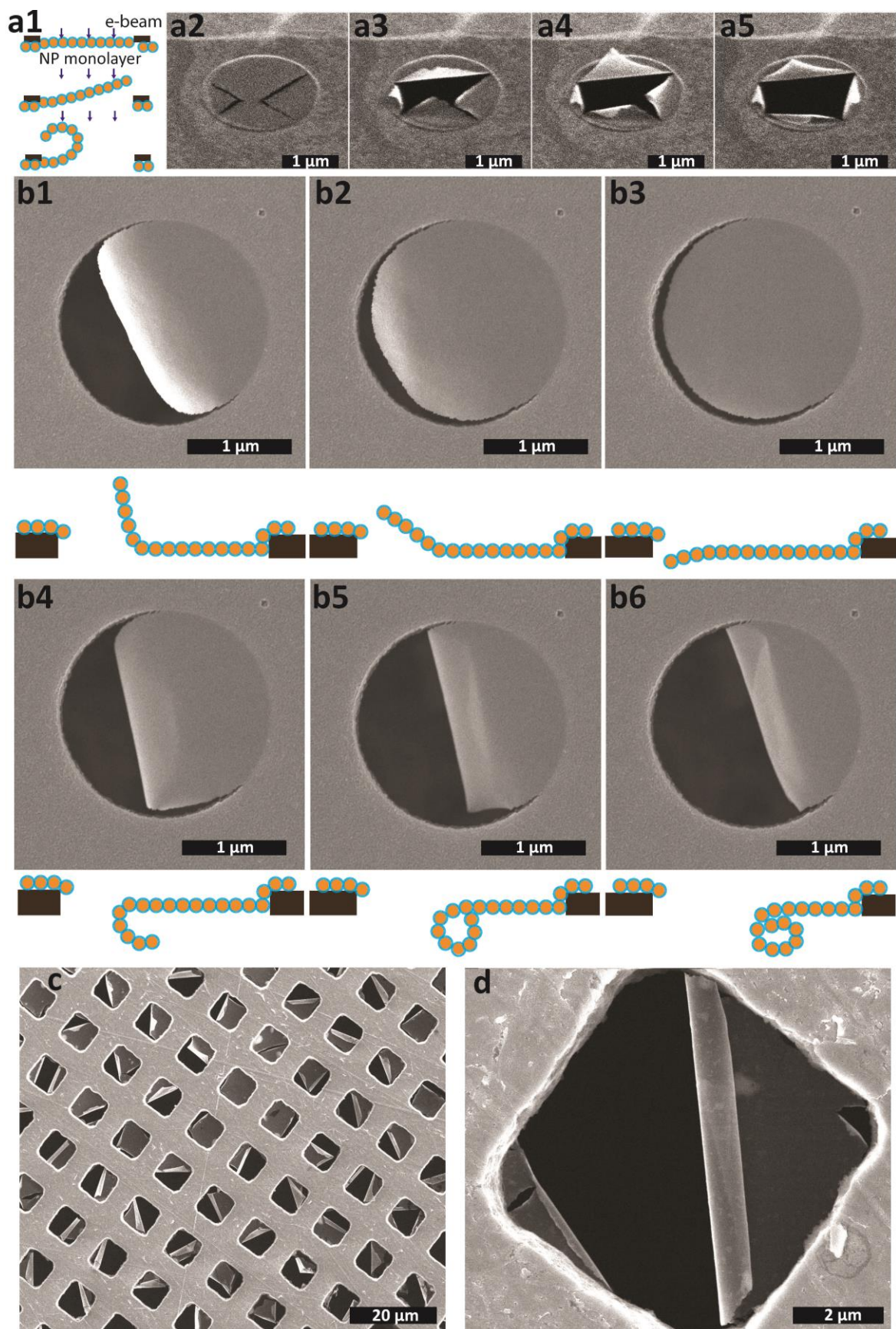
Figure 5. (a1) Sketch of the freestanding monolayer rolling towards the water-facing side under electron beam irradiation. (a2-5) SEM images of freestanding monolayer comprised of 5.2 nm Au-dodecanethiol nanoparticles draped over a 2µm hole in a carbon-coated TEM grid. An x-shaped slit has been cut by FIB and the membrane has been exposed to SEM electron beam scans 1, 8, 15 and 22 times (left to right). (b1-6) Sequence of SEM scans showing bending and nano-scroll formation of 5.2 nm Au-dodecanethiol monolayer membrane during e-beam exposure. Sketches underneath the images indicate the process. (c) SEM image of freestanding 5.2 nm Au-dodecanethiol monolayers on a copper TEM grid with 7.5µm square holes, after exposure to the e-beam for 30s. (d) Zoomed in image of a nano-scroll from panel (c).

To enable this curling process, the membrane has to be able to move and contract. In Figs. 5a2-5a5 a freestanding nanoparticle monolayer was first cut by a focused ion beam (FIB), producing an "X" shape slit pattern, and then exposed to successive scans with the electron beam of a SEM. Each image is a single full-frame scan at acceleration voltage 10kV and beam current of ~50pA. Immediately after the FIB cut and the first SEM scan the monolayer is still flat, but with increasing e-beam dose it curls up more and more.

Figure 5b shows more explicitly how e-beam exposure exploits the ligand density asymmetry. In this sequence of six SEM scans, a circular monolayer membrane started out partially detached along its perimeter, with a nearly vertical flap that happened to be bent toward the side originally facing away from the water (in the image it faces toward the SEM's secondary electron detector and thus appears bright). Under increasing exposure, the flap is effectively undone by bending it back toward the water-facing side and then the flap portion continues to roll up into a tight scroll underneath the intact portion of the membrane.

While complicated FIB cut patterns together with appropriate (and perhaps locally varied) e-beam exposure dose should enable intricate folding patterns, for rolling monolayers into scrolls even a partial rip along the perimeter of the membrane often suffices, as Fig, 5b showed, since it can trigger further ripping as the layer curls up. The most straightforward way to achieve this at high yield without even employing the FIB is to use holes with larger diameters, such as TEM grids with 7.5µm square holes. Given the longer perimeter, there is a higher probability that a

defect or grain boundary resides right at the edge where the freestanding portion of the membrane is tied to the supporting substrate, a spot of high local stress and thus likely to fail first. Figures 5c&d show how this can quickly produce a variety of scroll shapes under e-beam exposure.

Spontaneous drying-induced scroll formation in the absence of e-beam assistance occurred only rarely with appreciable yield, possibly because this requires a rather specific combination of drying conditions and ligand concentration in the nanoparticle solution. However, when adjusted properly, it is possible to find large areas in the substrate where arrays of membranes that initially covered holes have detached and self-rolled into nano-scrolls. Figure 7 shows results from one such experiment. Here the water droplet with the nanoparticle monolayer at its top interface was contained inside a cone-shaped support fabricated from PTFE. The substrate, a carbon-coated TEM grid (Quantifoil 657-200-CU) containing a regular array of 2μm diameter holes, was clamped between the PTFE holder and its aluminum counterpart (Fig. 6a).
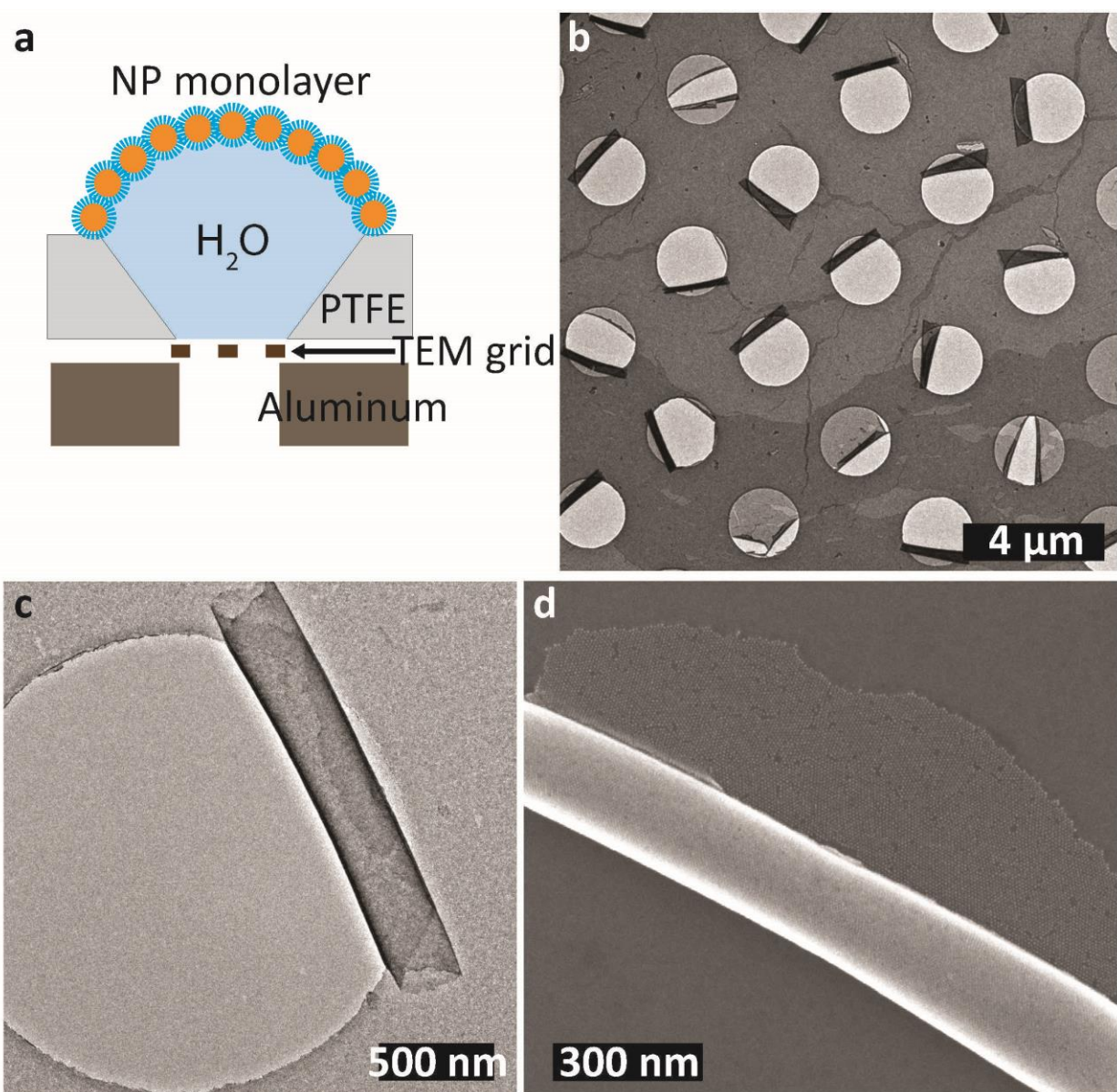
Figure 6. (a) Schematic of nanoparticle scroll assembly and transfer process. (b) TEM image of nanoparticle scrolls formed on a carbon-coated TEM grid with 2µm diameter holes via sponateous self-rolling during the drying process. (c) Zoomed in TEM image of a nanoparticle scroll showing individual particles and the wall thickness. (d) SEM image of a nanoparticle scroll transferred onto a silane-coated silicon-nitride substrate.

A PDMS stamp was then used to pick up the scrolls from the TEM grid and transfer them onto silicon nitride substrates (coated with dodecyltrichlorosilane for better adhesion of the scrolls).

With an elastic modulus three orders of magnitude smaller than that of our nanoparticle membranes, PDMS can conform to the scrolls without damaging them. The distribution of diameters D of over 100 scrolls is shown in Fig. 7a, with a mean value of ~300 nm as measured by SEM. Typical lengths of scrolls are 1-2μm, depending on how far they rolled up. Given their geometry, most transferred scrolls had a wall thickness of 2-3 monolayers.

To characterize the scrolls' bending response, we performed AFM indentation measurements. From the slope of such curves the indentation stiffness k was calculated. An example of a typical force-indentation curve is given in Fig. 7b, showing a response that is linear within the resolution of our measurements. In all cases, the stiffness was measured along the scroll apex to avoid slip of the AFM tip; the force was limited so that the maximum indentation did not exceed 3-10nm, depending on the local stiffness, and thus was less than the wall thickness. The distribution of stiffness values obtained from the central part of different scrolls is shown in Fig. 7c.
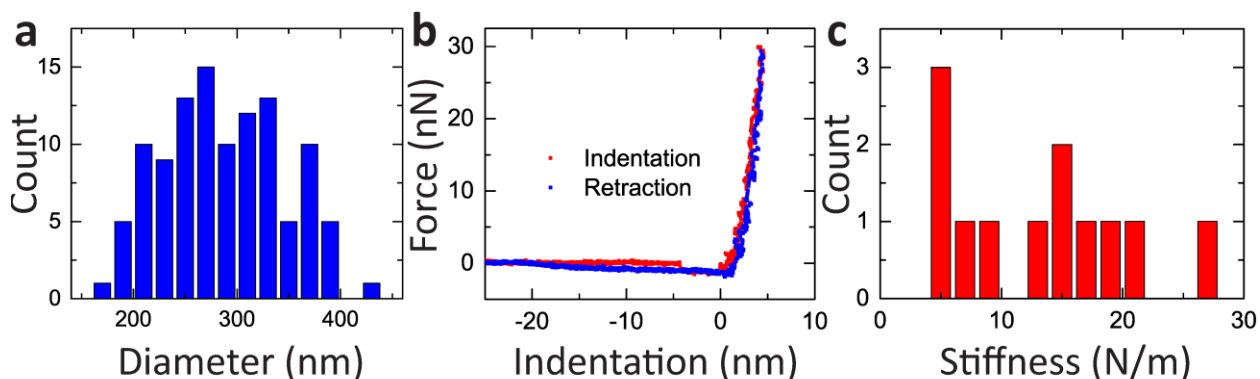
Figure 7 (a) Histogram of the diameter distribution for nanoparticle scrolls fabricated as shown in Fig. 6. (b) Typical force-indentation curve obtained by AFM. The tip comes is in contact with the scroll for positive indentation values. (c) Histogram of the stiffness values from the central region of different scrolls. All data are from scrolls fabricated with 5.2nm Au-dodecanethiol nanoparticles.

A most remarkable aspect emerging from these measurements is that the stiffness easily reaches values in the range of 10N/m even though the wall thickness is no more than 2-3 times the

monolayer thickness $t \approx$ 7nm. From prior measurements on flat monolayers under tensile stress, made of the same Au-dodecanethiol particles, we know that the Young's modulus E is around 2GPa, which gives an equivalent two-dimensional stretching modulus $E_{2D} = Et \approx$ 14 Pa m. For a thin long tube of effective wall thickness t_{eff} and radius R, standard elasticity theory would predict that, sufficiently far away from the ends, the indentation stiffness should scale as[42,43] $k \sim E_{2D}(t_{eff}/R)^{3/2}$, with a prefactor of order unity that depends on the Poisson ratio. Similarly, the bending modulus B should scale as $B \sim E_{2D}(t_{eff})^2$. If we take $t_{eff} = 3t = $ 21nm and an average radius $R = D/2 = $ 150nm to obtain an estimate for k we find $k \approx$ 0.9N/m. This is a factor of 5 lower than the smallest measured k (Fig. 7c) and a factor $\sim$10 lower than the stiffness in Fig 7b. It implies that, effectively, the scrolls behave as if their wall thickness was significantly thicker: matching the measured stiffness requires t_{eff} values that are 3-8x the physical wall thickness. Since the bending modulus B scales as $(t_{eff})^2$, the same reasoning suggests that B in our scrolls is enhanced by 1-2 orders of magnitude over the value predicted by classical continuum elastic model using the physical thickness.

4. Conclusions

Understanding the unique mechanical properties of ultrathin nanoparticle-based films and membranes is critical for using these materials in applications such as deformable electronics or mechanical actuators. We reported here on two aspects: the tensile strength and the bending stiffness. We studied the in-plane strength of nanoparticle monolayers and multilayers by investigating the micro-crack patterns resulting from applying controlled amounts of strain. From the distribution of fragment widths, we obtained information about the bond strength between neighboring nanoparticles and its distribution. Secondly, we discussed several methods to bend and curl initially flat nanoparticle membranes into hollow, three-dimensional structures, including combinations of ion beam cutting and electron beam irradiation. AFM measurements used to obtain bending modulus of rolled-up monolayer membranes showed that these structures respond to indentation in a manner that makes them appear significantly thicker, and thus stiffer, than expected based on their physical thickness.

Acknowledgements

References:

1. Shevchenko, E. V.; Talapin, D. V.; Kotov, N. A.; O'Brien, S.; Murray, C. B. *Nature* **2006**, 439,55– 59

2. Dong, A.; Chen, J.; Vora, P. M.; Kikkawa, J. M.; Murray, C. B. *Nature* **2010**, 466, 474-477

3. Cheng, W. L.; Campolongo, M. J.; Cha, J. J.; Tan, S. J.; Umbach, C. C.; Muller, D. A.; Luo, D. *Nat. Mater.* **2009**, 8, 519-525

4. Cheng, W. L.; Campolongo, M. J.; Cha, J. J.; Tan, S. J.; Umbach, C. C.; Muller, D. A.; Luo, D. *Nano Today* **2009**, 6, 482-493

5. Liao, J.; Zhou, Y.; Huang, C.; Wang, Y.; Peng, L. *Small* **2011**, 7, 583-587

6. Panthani, M. G.; Korgel, B. A. *Annu. Rev. Chem. Biomol. Eng.* **2012**, 3, 287-311

7. van Rijn, P.; Tutus, M.; Kathrein, C.; Zhu, L. L.; Wessling, M.; Schwaneberg, U.; Boker, A. *Chem. Soc. Rev.* **2013**, 42, 6578-6592

8. Yan, C.; Arfaoui, I.; Goubet, N.; Pileni, M.-P. *Adv. Funct. Mater.* **2013**, 23, 2315-2321

9. Gauvin, M.; Wan, Y.; Arfaoui, I.; Pileni, M.-P *J. Phys. Chem. C* **2014**, 118, 5005-5012

10. Jeong, Y.; Chen, Y.-C.; Turksoy, M. K.; Rana, S.; Tonga, G. Y.; Creran, B.; Sanyal, A.; Crosby, A. J.; Rotello, V. M. *Adv. Mater.* **2014**, 26, 5056-5061

11. Lane, J. M. D.; Grest, G. S. *Nanoscale* **2014**, 6, 5132-5137

12. Min, Y.; Akbulut, M.; Kristiansen, K.; Golan, Y.; Israelachvili, J. *Nat. Mater.* **2008**, 7,527

13. Nie, Z.; Petukhova, A.; Kumacheva, E. *Nat. Nanotechnol.* **2010**, 5, 15

14. Geim, A. K., Novoselov, K. S. *Nat. Mater.* **2007**, 6, 183-191

15. Bishop, K.J.M., Wilmer, C.E., Soh, S., Grzybowski, B. A. *Small* **2009**, 5, 1600-1630

16. He, J.; Lin, X. M.; Chan, H.; Vukovic, L.; Kral, P.; Jaeger, H. M. *Nano Lett.* **2011**, 11, 2430–2435

17. Kanjanaboos, P.; Lin, X. M.; Sader, J. E.; Rupich, S. M.; Jaeger, H. M.; Guest, J. R. *Nano Lett.* **2013**, 13, 2158-2162.

18. Talapin, D. V., Murray C. B. *Science* **2005**, 310, 86-89

19. Griffith, A. A. *Philos. Trans. R. Soc. London, Ser. A* **1921**, 221, 163

20. Thomson, R. M. *J. Phys. Chem. Solids* **1987**, 48, 965– 983

21. Hutchinson, J. W.; Suo, Z. *Adv. Appl. Mech.* **1992**, 29, 63

22. Fineberg, J.; Marder, M. *Phys. Rep.* **1999**, 313, 1– 108

23. Bouchbinder, E.; Fineberg, J.; Marder, M. *Annu. Rev. Condens. Matter Phys.* **2010**, 1, 371–395

24. Long, R.; Hui, C.-Y.; Cheng, W.; Campolongo, M.; Luo, D. *Nanoscale Res. Lett.* **2010**, 5, 1236-1239

25. Cox, B. N.; Gao, H.; Gross, D.; Rittel, D. *J. Mech. Phys. Solids* **2005**, 53, 565-596

26. Jiang Z.; He, J.; Deshmukh, S. A.; Kanjanaboos, P.; Kamath, G.; Wang, Y.; Sankaranarayanan S. R. S.; Wang, J.; Jaeger, H. M.; Lin, X. M. **2014**, submitted to Nature

27. Kanjanaboos, P.; Joshi-Imre, A.; Lin, X. M.; Jaeger, H. M. *Nano Lett.* **2011**, 11, 2567-2571

28. Zharnikov, M.; Grunze, M. *JSVT B* **2002**, 20, 1793-1807

29. Zhou, C.; Trionfi, A.; Hsu, J.W.P.; Walker, A.V. *J. Phys. Chem. C* **2010**, 114, 9362-9369

30. Mueggenburg, K. E.; Lin, X. M.; Goldsmith, R. H.; Jaeger, H. M. *Nat. Mater.* **2007**, 6, 656–660

31. He, J.; Kanjanaboos, P.; Frazer, N. L.; Weis, A.; Lin, X. M.; Jaeger, H. M. *Small* **2010**, 6,1449– 1456

32. Lin, X. M.; Jaeger, H. M.; Sorensen, C. M.; Klabunde, K. J. *J. Phys. Chem. B* **2001**, 105,3353– 3357

33. Liao, J. H.; Bernard, L.; Langer, M.; Schönenberger, C.; Calame, M. *Adv. Mater.* **2006**, 18,2444

34. Heinrich, M.; Gruber, P.; Orso, S.; Handge, U. A.; Spolenak, R. *Nano Lett.* **2006**, 6, 2026–2030

35. Sun, J. Y.; Lu, N. S.; Yoon, J.; Oh, K. H.; Suo, Z. G.; Vlassak, J. J. *J. Appl. Phys.* **2012**, 111,013517

36. Chung, J. Y.; Lee, J. H.; Beers, K. L.; Stafford, C. M. *Nano Lett.* **2011**, 11, 3361– 3365

37. Handge, U. A. *J. Mater. Sci.* **2002**, 37, 4775– 4782

38. Bazhenov, S. L.; Volynskii, A. L.; Alexandrov, V. M.; Bakeev, N. F. *J. Polym. Sci., Part B* **2002**, 40, 10– 18

39. Begley, M. R.; Bart-Smith, H. *Int. J. Solids Struct.* **2005**, 42, 5259– 5273

40. Wang, Y.; Kanjanaboos, P.; Barry, E.; Mcbride, S.; Lin, X. M.; Jaeger, H. M. *Nano Lett.* **2014**, 14, 826-830

41. Cordill, M. J.; Taylor, A.; Schalko, J.; Dehm, G. *Metall. Mater. Trans. A* **2010**, 41A,870

42. Pablo, P. J.; Schaap, I. A. T.; Mackintosh, F. C.; Schmidt, C. F. *Phys. Rev. Lett.* **2003**, 91, 098101.

43. Schaap, I. A. T.; Carrasco, C.; Pablo, P. J.; MacKintosh, F. C.; Schmidt, C. F. *Biophys. J.* **2006**, 91, 1521-1531